Ion-beam machining of millimeter scale optics

Prashant M. Shanbhag, Michael R. Feinberg, Guido Sandri, Mark N. Horenstein, and
Thomas G. Bifano

An ion-beam microcontouring process is developed and implemented for figuring millimeter scale optics. Ion figuring is a noncontact machining technique in which a beam of high-energy ions is directed toward a target substrate to remove material in a predetermined and controlled fashion. Owing to this non-contact mode of material removal, problems associated with tool wear and edge effects, which are common in conventional machining processes, are avoided. Ion-beam figuring is presented as an alternative for the final figuring of small (<1-mm) optical components. The depth of the material removed by an ion beam is a convolution between the ion-beam shape and an ion-beam dwell function, defined over a two-dimensional area of interest. Therefore determination of the beam dwell function from a desired material removal map and a known steady beam shape is a deconvolution process. A wavelet-based algorithm has been developed to model the deconvolution process in which the desired removal contours and ion-beam shapes are synthesized numerically as wavelet expansions. We then mathematically combined these expansions to compute the dwell function or the tool path for controlling the figuring process. Various models have been developed to test the stability of the algorithm and to understand the critical parameters of the figuring process. The figuring system primarily consists of a duo-plasmatron ion source that ionizes argon to generate a focused ($\sim$200-μm FWHM) ion beam. This beam is rastered over the removal surface with a perpendicular set of electrostatic plates controlled by a computer guidance system. Experimental confirmation of ion figuring is demonstrated by machining a one-dimensional sinusoidal depth profile in a prepolished silicon substrate. This profile was figured to within a rms error of 25 nm in one iteration. © 2000 Optical Society of America

OCIS codes: 220.1000, 220.4610.

1. Introduction

Rapid growth in the photonics industry, led by products such as fiber optics, compact disc players, and semiconductor lasers, has created a need for small-scale (<1-mm) contoured aspherical components. Although certain techniques exist for contouring optics on the centimeter scale and higher, to our knowledge no precise, controllable, and robust process has yet been developed for shaping millimeter scale optics. These optics include individual components such as lenses and mirrors for optical fiber interfaces, intraocular lenses, and arrays of microlenses and micromirrors used for adaptive optics and flat panel displays. The development of cost-effective techniques to make millimeter scale optics with custom surface contours is a critical need for emerging photonics applications. In this paper, ion-beam figuring is presented as a technique for imparting custom aspherical contours to a broad range of millimeter scale optics.

A. Overview of Ion Figuring

Ion figuring is performed with a beam of high-energy ions directed toward a target substrate in a predictable and controllable way. As shown in Fig. 1, ions sputter the substrate on impact—breaking surface bonds and removing material in molecular units. When a compact beam is rastered across a substrate, a complex contour can be generated. The depth of material removed by an ion beam can be found as the convolution between an ion-beam shape and an ion-beam dwell function, defined over a two-dimensional area of interest. In the process described in this paper, the beam dwell function is computed for a desired material removal contour and a known steady beam shape. The dwell function is computed through deconvolution. A wavelet-based algorithm has been developed to model the deconvolution process. The computed dwell function provides a prescribed tool path for controlling the figuring process.

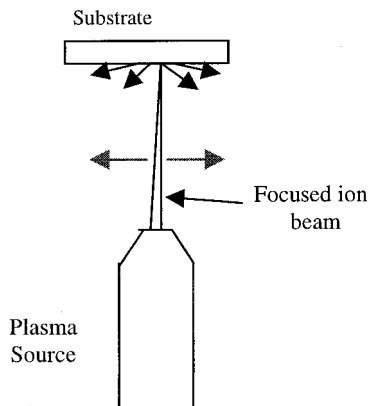Experimentally, ion figuring is performed by ras-

Fig. 1. Ion-figuring process.

tering a focused ion beam over a workpiece surface. Rastering is implemented with an orthogonal set of electrostatic plates through which the beam passes on its way through the ion source. The electrostatic plates are controlled by a computer guidance system in accordance with the desired dwell function.

The ion-figuring system used in this research comprises a duo-plasmatron ion source that generates a 3-keV argon-ion beam with a beam current of ~0.5 μA. Charged ions are accelerated by an electrostatic field and focused with electrostatic lenses to form a focused ion beam. Accelerated ions break the interatomic bonds of the target substrate on striking it and thus sputter material off the surface. The beamwidth can be varied from ~75-μm FWHM to ~200 μm, and peak removal rates can be varied from 25 to 200 nm/min. This is typically done by varying the input voltages to the source and focusing optics and by controlling the gas (argon) flow rate.

Material removal is spatially controlled by either moving the beam with respect to the substrate or vice versa. Figuring is performed in a chamber under moderate vacuum ($\sim 1.3 \times 10^{-5}$ Torr). The ion beam shape and peak removal rate remain approximately constant over the entire machining period, so the material removed from the substrate can be found as a convolution of a fixed beam profile and beam dwell function.

An important feature of ion figuring compared with other material removal processes is that the optical substrate is loaded only by a molecular-scale impact during machining, and this load is orders of magnitude smaller than that required for conventional polishing or grinding. Therefore problems associated with tool wear and edge effects, which are common in grinding and polishing, are eliminated. Additionally, since the substrate is not clamped during figuring, there is no postmachining workpiece distortion resulting from the relaxation of clamping stresses.

B.   Background of Ion Figuring

Wilson et al.[1,2] pioneered the ion-figuring technique by machining 30-cm optical flats of fused silica from an initial surface error of 0.41λ rms (λ = 633 nm) to a final figure of 0.042λ rms in one iteration. They

used 1.5-keV argon ions at a 40-mA current produced by a 2.54-cm Kaufman ion source. The entire machining was performed in 5.5 h. A deconvolution algorithm based on Fourier transform, specifically developed for the technique, accurately predicted the desired material removal.

Allen and Keim[3] reported the ion-figuring capability for correcting symmetric and asymmetric figure error on polished glass aspheric substrates. Ion figuring was used to correct axisymmetric figure errors to less than 0.010λ rms. In this approach an aperture was designed based on the residual radial error profile of the optic and a known ion-beam removal rate.

Subsequently Allen et al.[4–6] and Pileri[7] successfully corrected the residual surface figure error on a 1.8-m Zerodur off-axis segment of the Keck telescope primary mirror. The mirror blank was preprocessed by the bend-and-polish technique[8] and finally cut to the desired hexagonal shape, which left significant postmachining figure errors (3.13 μm peak to valley, 0.726 μm rms). The mirror surface was ion figured in a 2.5-m ion-figuring system with a 2.54-cm broadbeam source in two iterations. The surface figure error was reduced from 0.726 to 0.252 μm rms in the first iteration and then to 0.090 μm rms in the final step.

Drueding et al.[9–12] developed an ion-figuring system for centimeter-size fused silica and chemical-vapor-deposited SiC samples optics. The process was demonstrated by figuring various spherical, parabolic (both concave and convex), flat, and saddle shapes in these substrate materials. A parabola of 1-m radius was figured in a fused silica substrate, from an initial error of 1138–80 nm (rms) in one iteration. Similarly, a SiC saddle was figured from an initial error of 982–324 nm (rms) in one step.

It can be observed that previous efforts in ion figuring have been concentrated toward machining optical components with characteristic dimensions of the order of a few centimeters and higher. In the research presented in this paper, ion figuring has been used to impart custom aspherical contours to millimeter scale optics. Figuring is performed by rastering a focused ion beam (typical sizes used are 50–200 μm) over a stationary target substrate.

2.   Mathematical Model of the Figuring Process

A convolution model is used to describe the ion-figuring process. In this model the following assumptions have been made. All have been verified, to first order, by empirical results.

• The beam function (the material removal profile of the ion beam) is fixed. It is the same at all locations and times during the figuring process.
• Material removal is isotropic and proportional to dwell time.
• The beam function is insensitive to rastering position.

For a given initial surface $I(x, y)$ and a desired final surface $F(x, y)$, the removal function $R(x, y)$ is obtained by subtracting the initial surface from the final surface. This removal surface is machined with an ion beam having a material removal function or a beam function $B(x, y)$. The beam function is governed by the physical parameters of the figuring system. The dwell function $D(x, y)$ is computed by deconvolving $B(x, y)$ from $R(x, y)$. The dwell function $D(x, y)$ is the map of dwell times per unit area for which the beam is held stationary at each point (x, y) during its sweep over the removal surface.

The ion-figuring process can be represented in two dimensions:

$$R(x, y) = \int_{-\infty}^{\infty} \int_{-\infty}^{\infty} B(x - x', y - y') D(x', y') dx' dy'. \tag{1}$$

The total work space is broken into square grids of unit area, and the beam is positioned at the center of each area for a time approximately equal to the product of the computed dwell function at the square's coordinates (x, y) and the area of the square A_{ij}.

Thus a dwell time at

$$i, j = \iint_{A_{ij}} D(x, y) dx dy$$
$$\approx D(x_i, y_j) \Delta x_i, \Delta y_j. \tag{2}$$

This relationship allows us to express Eq. (1) in discretized form as

$$R(x, y) = \sum_{i=0}^{m-1} \sum_{j=0}^{m} B(x - x_i, y - y_j) D(x_i, y_j) \Delta x_i \Delta y_j. \tag{3}$$

This discretization of the removal function suggests that the figuring process can be discretized in a similar way, thereby representing the removal process as a discrete two-dimensional (2-D) convolution.

Since the contour figured by the ion beam is equal to the convolution of a fixed beam profile and a beam dwell function, i.e., $R = B * D$, computation of the corresponding dwell function from the desired removal and the fixed beam function is a deconvolution process.

A. Earlier Methods

Wilson et al.[2] used Fourier techniques to perform the deconvolution operation. Convolution of the two functions in the spatial domain can be expressed as a product of their spatial Fourier transforms in the spatial-frequency domain, e.g.,

$$\tilde{R} = \tilde{B} \cdot \tilde{D}, \tag{4}$$

where in this case $\tilde{R}$ is the spatial Fourier transform of the removal function, $\tilde{B}$ is the spatial Fourier transform of the beam function, and $\tilde{D}$ is the spatial Fourier transform of the dwell function.

Thus in the Fourier implementation of the computation of the dwell function simply involves dividing the Fourier transform of the removal function by the Fourier transform of the beam function and taking the inverse Fourier transform of the result:

$$\tilde{D}(x, y) = F^{-1}\{\tilde{R}(k_x, k_y) \cdot \tilde{B}^{-1}(k_x, k_y)\}. \tag{5}$$

The deconvolution step in Eq. (5) is numerically unstable. This instability can best be explained by examining the case of a one-dimensional (1-D) Gaussian beam function. The Fourier transform of a Gaussian, e.g., $B(x) = \exp(-x^2/\lambda^2)$, is itself a Gaussian, $\tilde{B}(k) = \exp(-k^2\lambda^2/4)$, where k is the spatial frequency in the Fourier space and λ is the $1/e$ width of the Gaussian function. The inverse Fourier transform of this function represented by Eq. (5) is divergent because the denominator approaches zero for large values of k_x and k_y. Wilson et al.[2] resolved this problem with a threshold inverse filter.

Allen and Romig[4] have demonstrated an iterative method for finding a solution to the dwell function. In this method a smart guess is made for the dwell function (often by setting it equal to the desired removal function) to compute the convolution. The difference between the result of the convolution and the actual removal function is then used for successive iterations. The computation is repeated until the solution converges to within the acceptable limits of error. Simply, this iterative process can be expressed as

$$D_{n+1} = D_n + k(R - B*D_n). \tag{6}$$

Stability is always a concern in iterative techniques, and the experience of Allen et al.[6] indicates that these methods sometimes fail to converge. Nevertheless this approach is quite attractive for its simplicity and has met with considerable success in practice.

Figuring work reported by Carnal et al.[13] is based on a matrix algebraic approach that requires inversion of the beam function matrix:

$$D(x, y) = R(x, y) B(x, y)^{-1}, \tag{7}$$

where $D(x, y)$, $R(x, y)$, and $B(x, y)$ are the dwell, removal, and beam function matrices, respectively. Matrix inversion becomes problematic when the beam function becomes sparse and highly singular. The requirements of square function matrices pose similar problems, as in the Fourier approach. Single-valued decomposition methods were used to construct the solution.

B. Wavelet Algorithm

In this paper a novel wavelet-based algorithm has been presented to model the deconvolution operation. In the wavelet algorithm, each element of the convolution, i.e., the removal function $R(x, y)$, beam function $B(x, y)$, and the dwell function $D(x, y)$ is synthesized by a wavelet series expansion.

For example, the removal function $R(x, y)$ can be expressed as

$$R(x, y) = \sum_{n=0}^{\infty} \sum_{m=0}^{\infty} r_{nm}^{(\lambda_{Rx}, \lambda_{Ry})} \delta_{\lambda_{Rx}}{}^n(x) \delta_{\lambda_{Ry}}{}^m(y), \tag{8}$$

where $\delta_{\lambda_{Rx}}{}^{n}(x)$ is the nth derivative of the Gaussian along x for $\lambda = \lambda_{Rx}$; $\delta_{\lambda_{Ry}}{}^{m}(y)$ is the mth derivative of the Gaussian along y for $\lambda = \lambda_{Ry}$; $r_{nm}{}^{(\lambda_{Rx}, \lambda_{Ry})}$ is the (n, m)th coefficient of the wavelet series expansion; and λ_{Rx}, λ_{Ry} are the widths of the fundamental wavelet along the x and y axes, respectively.

The first basis function of the wavelet series, which is the zeroth derivative of a Gaussian, is known as the fundamental wavelet of the series.

The nth derivative of a Gaussian can be computed with Rodriguez's formula[14]

$$\delta_{\lambda}{}^{n}(x) = (-1)^{n} H_{n}{}^{\lambda}(x) \delta_{\lambda}(x), \qquad (9)$$

where

$$\delta_{\lambda}(x) = \frac{\exp(-x^2/\lambda^2)}{\sqrt{\pi}\lambda} \qquad (10)$$

is the normalized Gaussian in x, $H_{n}{}^{\lambda}(x)$ is the nth (order) Hermite polynomial in x for a given λ, and λ is the width of the Gaussian.

Similarly, the beam function is written as

$$B(x, y) = \sum_{n=0}^{\infty} \sum_{m=0}^{\infty} b_{nm}{}^{(\lambda_{Bx}, \lambda_{By})} \delta_{\lambda_{Bx}}{}^{n}(x) \delta_{\lambda_{By}}{}^{m}(y), \quad (11)$$

where $b_{nm}{}^{(\lambda_{Bx}, \lambda_{By})}$ is the (n, m)th coefficient of $B(x, y)$ in its wavelet series expansion.

The series coefficients of the removal and beam functions, namely, r_{nm} and b_{nm}, respectively, are computed by using the orthonormality of the basis functions, e.g.,

$$r_{nm}{}^{(\lambda_{Rx}, \lambda_{Ry})} = \frac{(-1)^{n+m}(\lambda_{Rx})^{2n}(\lambda_{Ry})^{2m}}{2^{n} n! 2^{m} m!} \int_{-\infty}^{\infty} \int_{-\infty}^{\infty} R(x, y)$$

$$\times H_{n}{}^{\lambda_{Rx}}(x) H_{m}{}^{\lambda_{Ry}}(y) \mathrm{d}x \mathrm{d}y, \qquad (12)$$

where $H_{n}{}^{\lambda_{Rx}}(x)$ is the nth (order) Hermite polynomial in x for $\lambda = \lambda_{Rx}$ and $H_{m}{}^{\lambda_{Ry}}(y)$ is the mth (order) Hermite polynomial in y for $\lambda = \lambda_{Ry}$.

The basis functions and the series coefficients of the removal and beam functions are related to the dwell function. The fundamental wavelet widths of the dwell function are calculated as

$$\lambda_{Dx}{}^{2} = \lambda_{Rx}{}^{2} - \lambda_{Bx}{}^{2}, \qquad (13)$$

$$\lambda_{Dy}{}^{2} = \lambda_{Ry}{}^{2} - \lambda_{By}{}^{2}. \qquad (14)$$

The d_{nm} coefficients of the dwell function are computed by using the deconvolution algebra, which is developed in Subsection 2.3.

Using the d_{nm} coefficients and the widths of the basis functions, we synthesize the dwell function as follows:

$$D(x, y) = \sum_{n=0}^{\infty} \sum_{m=0}^{\infty} d_{nm}{}^{(\lambda_{Dx}, \lambda_{Dy})} \delta_{\lambda_{Dx}}{}^{n}(x) \delta_{\lambda_{Dy}}{}^{m}(y), \quad (15)$$

where $d_{nm}{}^{(\lambda_{Dx}, \lambda_{Dy})}$ is the (n, m)th coefficient of $D(x, y)$ in its wavelet series expansion.

C. Advantages of the Wavelet Technique

The wavelet technique offers the following advantages:

- For the shapes that are commonly encountered in this research, namely, sinusoids and Gaussians, wavelets are efficient. The beam function $B(x, y)$, for example, has a Gaussianlike distribution that can be synthesized accurately by using the Gaussian basis of the wavelet expansion in relatively few terms.
- The deconvolution process (as is evident in Subsection 2.E) is reduced to straightforward algebra, which can be efficiently programmed on a computer.

D. Computation of Convolution and Deconvolution with Gaussian Wavelets

In this subsection the wavelet deconvolution algebra is developed for one-dimensional functions. One-dimensional functions have been used for mathematical convenience, and a similar analysis leads to the algebra for 2-D deconvolution.

Consider the following 1-D convolution:

$$h(x) = \int_{-\infty}^{\infty} f(x - y) g(y) \mathrm{d}y. \qquad (16)$$

The deconvolution algebra starts with the 1-D wavelet expansions of the above functions, namely, f, g, and h. The goal is to come up with an expression that relates the wavelet expansion coefficients of these functions, i.e., to express c_s in terms of a_n and b_m:

$$f = \sum_{n=0}^{\infty} a_{n} \delta_{1}{}^{(n)}, \qquad (17)$$

$$g = \sum_{m=0}^{\infty} b_{m} \delta_{2}{}^{(m)}, \qquad (18)$$

$$h = \sum_{s=0}^{\infty} c_{s} \delta_{3}{}^{(s)}. \qquad (19)$$

Using the algebraic properties of the convolution product yields

$$f * g = \left[\sum_{n} a_{n} \delta_{1}{}^{(n)} \right] * \left[\sum_{m} b_{m} \delta_{2}{}^{(m)} \right] \qquad (20)$$

$$= \sum_{n} \sum_{m} a_{n} b_{m} [\delta_{1}{}^{(n)} * \delta_{2}{}^{(m)}] \qquad (21)$$

$$= \sum_{n} \sum_{m} a_{n} b_{m} \delta_{3}{}^{(n+m)}. \qquad (22)$$

Rearranging the double sum by first changing the summation variable and then interchanging the order of summation, we have the following:

(1) Change of variables ($m \to s$ for fixed n) i.e., let $n + m = s$ so $(n, m) \to (n, s)$

$$f * g = \sum_{n=0}^{\infty} \sum_{s=n}^{\infty} a_{n} b_{s-n} \delta_{3}{}^{(s)}. \qquad (23)$$

(2) Interchange the order of summation ensuring that the domain is preserved, i.e.,

$$f*g = \sum_{n=0}^{\infty} \sum_{s=n}^{\infty} a_n b_{s-n} \delta_3^{(s)} \qquad (24)$$

$$= \sum_{s=0}^{\infty} \sum_{n=0}^{s} a_n b_{s-n} \delta_3^{(s)} \qquad (25)$$

$$= \sum_{s=0}^{\infty} \delta_3^{(s)} \left(\sum_{n=0}^{s} a_n b_{s-n} \right). \qquad (26)$$

Comparing this with Eq. (19) shows

$$c_s = \sum_{n=0}^{s} a_n b_{s-n}. \qquad (27)$$

In terms of n, vectors $\mathbf{a}$, $\mathbf{b}$, and $\mathbf{c}$ that represent the sets of coefficients a_n, b_n, and c_n can be written as

$$c = a*b. \qquad (28)$$

Writing out Eq. (28) explicitly for $n = 0$, 1, and 2 yields

$$c_0 = a_0 b_0, \qquad (29)$$

$$c_1 = a_0 b_1 + a_1 b_0, \qquad (30)$$

$$c_2 = a_0 b_2 + a_1 b_1 + a_2 b_0 \dots . \qquad (31)$$

To compute b_n from a_n and c_n, we rewrite the linear system of Eqs. (28)–(31) are rewritten as

$$b_0 = c_0/a_0, \qquad (32)$$

$$b_1 = (-c_0 a_1 + c_1 a_0)/a_0^2, \qquad (33)$$

$$b_2 = (c_0 a_1^2 - (c_0 a_2 + c_2 a_1)a_0 + c_2 a_0^2)/a_0^3. \qquad (34)$$

Equation (28) can be conveniently written in recursive form to obtain successive b_n coefficients:

$$b_n = \left[c_n - \sum_{m=0}^{n-1} a_{(n-m)} b_m \right] \Big/ a_0. \qquad (35)$$

A similar analysis leads to the $b_{n,m}$ coefficients for the 2-D case and is given as follows:

$$b_{n,m} = (c_{n,m} - M - N - O)/a_{0,0}, \qquad (36)$$

where

$$M = \sum_{x=0}^{n-1} \sum_{y=0}^{m-1} a_{(n-x, m-y)} b_{(x,y)}, \qquad (37)$$

$$N = \sum_{x=0}^{n-1} a_{(n-x, 0)} b_{(x,m)}, \qquad (38)$$

$$O = \sum_{y=0}^{m-1} a_{(0, m-y)} b_{(n,y)}. \qquad (39)$$

E. Steps of the Algorithm

In this subsection we describe the step-by-step deconvolution procedure for using the wavelet algorithm. The main inputs to the algorithm are the initial surface contour and the beam distribution profile or the beam function. The removal function $R(x, y)$ is obtained by subtracting the initial surface map from the desired surface map. The algorithm then computes the dwell time map by deconvolving the beam function $B(x, y)$ from the removal function $R(x, y)$.

The algorithm has been numerically implemented and tested in Matlab and its output is interfaced to the ion gun controller of the duo-plasmatron by Lab-View.

1. Measure the Beam Function $B(x, y)$

For a figuring system the first task is to measure the beam function $B(x, y)$, which provides the depth removal rate of the beam as a function of the radial distance from its center. This can be easily determined by machining a hole in a flat substrate for a known time period. The beam function is typically Gaussianlike in distribution and is characterized by its FWHM and maximum removal rate. The beamwidth is directly measured from the depth profile, and the maximum removal rate is calculated by dividing the maximum depth of the hole by the overall machining time. The beam profile and beam current strongly depend on parameters such as the type of ion source, voltage inputs to the source and focusing optics, base and operating pressures inside the machining chamber, and type and quality of the gas. Historically, Kauffman-type[15] filament ion sources have been used for figuring centimeter-size optics. Since the working area in this research was an order of magnitude smaller, we needed a source that could generate a narrow ($\sim$200-μm FWHM) focused beam. So a duo-plasmatron ion source (donated by Oryx Instruments, Fremont, Calif.) was used. In this source the plasma is generated in two regions: the low-density cathode plasma between the cathode and an intermediate electrode and the high-density region between the intermediate electrode and anode. The accelerated ions are subsequently focused into a narrow beam with electrostatic lenses. This source can generate ion beams with 3–5 keV and sizes varying from 50 to 200 μm (FWHM) at beam currents of approximately 0.5–2 μA.

An optimum combination of these various parameters produces a stable beam profile. Once a satisfactorily stable beam is obtained, these settings are recorded to reproduce the same profile for subsequent machining. A detailed description of the different beam parameters and the method to obtain a stable beam is included in Subsection 4.A.

2. Measure the Removal Function $R(x, y)$

The removal function $R(x, y)$ is obtained by subtracting the initial height map $I(x, y)$ of the optical surface from the final desired surface $F(x, y)$. The initial map is measured with any suitable metrology technique such as interferometry and surface profilometry. The work space is discretized into small squares of equal area, and the surface height is given at the center of each square:

$$R(x, y) = F(x, y) - I(x, y). \qquad (40)$$

3. Offset the Removal Function

The removal map as obtained from the interferometer has positive and negative heights with respect to a zero reference. Because ion machining can only remove material, it is important that the removal function have only positive values. So the dataset is offset by a suitable value. A large offset is undesirable since more terms are necessary to map the function. Typically this value is selected so that the minimum value of the function is zero.

4. Attach a Taper along the Edges of the Removal Function

The removal function has a finite boundary where the function is not necessarily zero. To eliminate deconvolution problems resulting from sharp discontinuities at the edges, the function is artificially tapered all along its boundary. Since the basis functions of the wavelet expansions are Gaussians and their derivatives, a Gaussian function was chosen for the taper. The wavelet expansion can fit a Gaussian edge more effectively than it can fit any other form of taper. This additional taper data fall outside the area of interest on the substrate.

Simulations with 1-D sinusoids revealed a correlation between the width of the Gaussian taper and the fundamental width of the wavelet expansion used to synthesize the function. The series converged best (the rms and local errors were used as metrics to test convergence) when the width of the Gaussian taper was ~75% of the width of the wavelet.

5. Synthesize the Removal and Beam Function with the Wavelet Expansion

The next step involves synthesizing the removal and the beam functions with Gaussian wavelets. This step includes selection of two important parameters of the wavelet expansion, namely, the fundamental width of the wavelet series and the number of terms of the expansion. The fundamental width of the wavelet series is the width of the zeroth derivative Gaussian (basis) function. The expansion coefficients are computed by using the orthonormality of the basis functions [see Eq. (15)]. The accuracy of the wavelet series with a certain number of expansion terms is characterized by the rms error. The rms error (for fitting the removal and beam functions in simulations) is the standard rms error and is defined (e.g., for the removal function) as follows:

$$\text{rms error} = \left[\frac{1}{N^2} \sum_{n,m=1}^{N} \{R_{\text{actual}}(x_n, y_m) - R_{\text{synthesized}}(x_n, y_m)\}^2 \right]^{1/2}, \quad (41)$$

where N is the total number of points along the X and Y axes, R_{actual} is the input removal function, and $R_{\text{synthesized}}$ is the removal function synthesized with the wavelet expansion.

6. Deconvolve

Using the wavelet deconvolution algebra developed in Subsection 2.D, we compute the series coefficients of the dwell function from the coefficients of the removal and beam function:

$$d_{n,m} = [r_{n,m} - P - Q - R]/b_{0,0}, \quad (42)$$

where

$$P = \sum_{x=0}^{n-1} \sum_{y=0}^{m-1} b_{(n-x,m-y)} d_{(x,y)}, \quad (43)$$

$$Q = \sum_{x=0}^{n-1} b_{(n-x,0)} d_{(x,m)}, \quad (44)$$

$$R = \sum_{y=0}^{m-1} b_{(0,m-y)} d_{(n,y)}, \quad (45)$$

and

$d_{n,m}$ is the (n, m)th series coefficient

of the dwell function; (46)

$b_{n,m}$ is the (n, m)th series coefficient

of the beam function; (47)

$r_{n,m}$ is the (n, m)th series coefficient

of the removal function. (48)

7. Synthesize the Dwell Function $D(x, y)$

The wavelet widths of the basis functions (λ_{Dx}, λ_{Dy}) used to synthesize the dwell function are computed as follows:

$$\lambda_{Dx}{}^2 = \lambda_{Rx}{}^2 - \lambda_{Bx}{}^2, \quad (49)$$

$$\lambda_{Dy}{}^2 = \lambda_{Ry}{}^2 - \lambda_{By}{}^2. \quad (50)$$

With the series coefficients $d_{n,m}$ and the fundamental widths (λ_{Dx}, λ_{Dy}), the dwell function $D(x, y)$ is synthesized as follows:

$$D(x, y) = \sum_{n=0}^{\infty} \sum_{m=0}^{\infty} d_{nm}{}^{(\lambda_{Dx}, \lambda_{Dy})} \delta_{\lambda_{Dx}}{}^n(x) \delta_{\lambda_{Dy}}{}^n(y). \quad (51)$$

This completes implementation of the wavelet-based deconvolution algorithm.

F. Using the Computed Dwell Function for Ion Figuring

The synthesized dwell function is interfaced to the controller of the duo-plasmatron source. A computer interface (designed in LabView) is built to control the ion source remotely. This interface controls voltage input to the electrostatic raster plates of the duo-plasmatron, thereby regulating the position of the beam. The beam is held at a (x, y) position for a time interval equal to the computed dwell time at that corresponding position, after which it moves on to the next position and so on.

3. Simulations

Various test cases were developed to identify the critical parameters of the figuring process, understand their interrelationship, and test the performance of the deconvolution algorithm. In addition to a better understanding of the figuring system, the models were also designed to set the theoretical limits of the figuring process. Both 1-D and 2-D models were developed and tested. The 1-D test models were analytically generated, while the actual surface of a nine-element continuous deformable micro-electromechanical systems (MEMs) mirror was used as a 2-D model. The deformable mirror[16] surface is approximately 850 μm × 850 μm and has a sinusoidal height variation.

The following terminology is used in the simulations.

• Lambda expansion λ_{expn} is the fundamental width of the wavelet series expansion (the width of the first basis function, which is also the zeroth Gaussian derivative, is the fundamental width of the series).
• Lambda taper λ_{taper} is the width of the Gaussian taper.
• F is the real input data or the input function.
• F_{check} is the data (function) synthesized with the wavelet series.
• Lambda function λ_{func} is the dominant period of the input function 'F'.
• N is the number of expansion terms in the wavelet series.

A. Relevance of the Various Terms of the Wavelet Expansion

A given function can be synthesized with Gaussian wavelets to within acceptable limits of error by selecting an arbitrary λ_{expn} (fundamental width of the wavelet series) and a large number of expansion terms. Alternatively, one can approximate that function by limiting the number of terms to a finite value and choosing an optimal width λ_{expn}. With the optimal λ_{expn} the wavelet expansion converges much faster than with an arbitrary width. Theoretically, λ_{expn} should be larger than the grid spacing (or the discretization length) used in figuring and less than the domain (or the support) of the function.

Generally, for a function with an inherent periodic surface height variation, the optimal value is found to be related to the dominant period of the function. The first choice of λ_{expn} for synthesizing such functions with the wavelet expansion is often the dominant period of the function itself.

In Subsection 3.B it is shown that for a 1-D sinusoidal function an optimal value of λ_{expn} exists that is related to the dominant period of the function λ_{func}. Similarly, for a sinusoidal function with a finite nonzero boundary, the relationship between the width of the Gaussian taper λ_{taper} and the dominant period of the function λ_{func} is deduced.
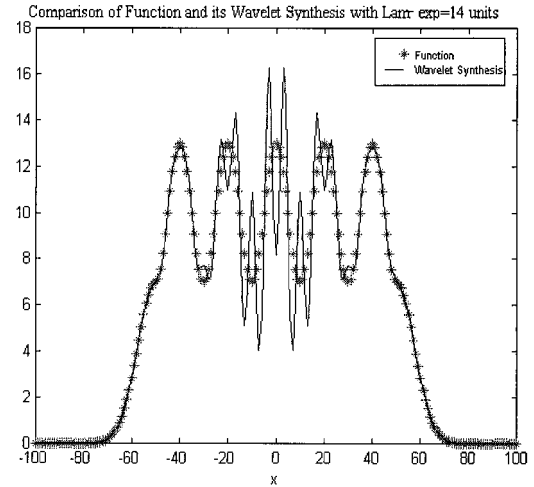
The results from the 1-D analysis of these sinusoi-

Fig. 2. Five-bump sinusoid mapped with $\lambda_{expn} = 14$ units and 85 terms.

dal functions are utilized for the synthesis of the real surface of a MEMS mirror in Subsection 3.C. The mirror surface spans over an area of approximately 850 μm × 750 μm and has an approximately sinusoidal height variation. The dwell function required for correcting the nonplanarity of this mirror surface with a 120-μm (FWHM) ion beam is also computed.

B. One-Dimensional Simulations

The wavelet algorithm was tested at various stages of its development. During the initial stages of the algorithm, 1-D models were developed and synthesized

• To optimize the selection of the parameters of the wavelet expansion, namely, the fundamental width of the wavelet series λ_{expn} and the number of terms in the expansion.

• To select an optimal width for the Gaussian taper λ_{taper}.

All parameters of the 1-D models are expressed in arbitrary units.

In this subsection λ_{expn} is optimized for a sinusoidal function with 5 bumps. The 5-bump model is a cosine function with an amplitude variation of 5 units, offset from zero by 10 units, and has a fluctuation period of 20 units (i.e., $\lambda_{func} = 20$ units).

Figure 2 shows the 5-bump model, synthesized with $\lambda_{expn} = 14$ units and 85 terms of the wavelet expansion. In Fig. 3, the wavelet expansion synthesizes the same function more accurately with $\lambda_{expn} = 19$ and the same number of expansion terms:

$$\text{optimal } \lambda_{expn} = (0.8 \text{ to } 1.1)\lambda_{func}.$$

Figure 4 shows the variation of the rms error with λ_{expn} for the 5-bump model. In general the error is minimized when $\lambda_{expn} \approx \lambda_{func}$.

Various 1-D simulations in addition to the example described here were performed. All had a dominant
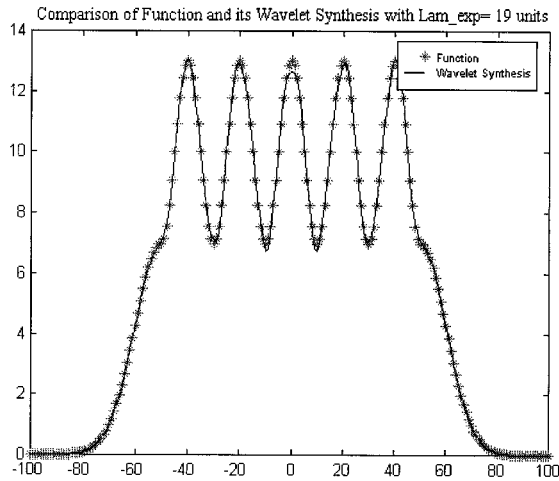
Fig. 3. Same five-bump sinusoid mapped more accurately with λ_{expn} = 19 units and 85 terms.

periodicity characterized by λ_{func}. The trends that were observed are as follows:

$\lambda_{taper} \approx 0.75\lambda_{func}$ provides the least-fitting error,

$\lambda_{expn} \approx \lambda_{func}$ provides the optimal synthesis.

More terms are necessary to synthesize the function with higher-frequency contour components.

C. Two-dimensional Simulations

The test model for 2-D simulation is the surface of a real nine-element continuous MEMS deformable mirror.[16] This mirror is a thin-film MEMS device that is used to correct wave-front aberrations in an adaptive optics application. During fabrication a complex stress gradient is induced along the thickness of the mirror membrane, which distorts the surface planarity when the device is released. The objective of this simulation is to compute the dwell function that can be used to planarize the mirror surface with a focused ion beam.
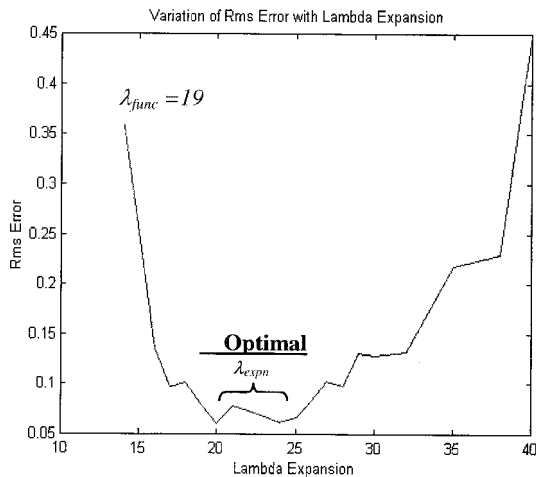
Fig. 4. Variation of rms error with λ_{expn}.
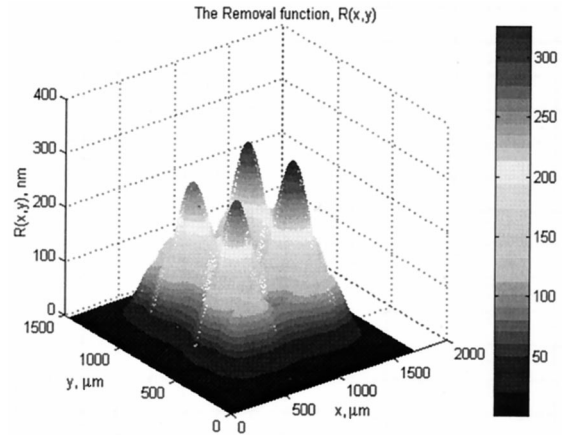
Fig. 5. Initial surface offset and tapered to obtain the removal function $R(x, y)$.

The dwell function has been computed for a relatively broad 120-μm (FWHM) ion beam. The narrowness or broadness of the ion beam is defined relative to the size of the features in the removal surface. Some interesting results are obtained when the beamwidth becomes comparable with the feature size of the removal function. These results are discussed in Subsection 3.C.3.

1. Synthesizing the Removal Function $R(x, y)$

The initial surface of the deformable mirror is measured interferometrically with a Phase Shift interferometer. Since the objective is to make this mirror surface flat, the initial measured contour is the removal function (with offset and taper added). Note that the surface points have been highly exaggerated along their Z axis for better visualization.

The surface has a sinusoidlike height variation with a dominant period of ~260 μm along the X axis and 200 μm along the Y axis. The maximum non-planarity of the surface is 325 nm. The surface spans an area of 850 μm × 750 μm. Based on the 1-D analysis in Subsection 3.B, the fundamental widths of the wavelet series (along the X and Y axes) are chosen as follows:

$$\lambda_{expn\_x} = 225 \ \mu m, \qquad \lambda_{expn\_y} = 195 \ \mu m.$$

To eliminate mapping difficulties due to sharp discontinuities at the finite boundary of the surface, we attach a Gaussian taper to its edges. The width of this Gaussian taper is also chosen based on 1-D analysis ($\lambda_{taper} = 0.75 \times \lambda_{expn}$). Thus $\lambda_{taper\_x} = 165 \ \mu m$ and $\lambda_{taper\_y} = 145 \ \mu m$ are chosen as the taper widths along the X and Y axes.

The removal function is synthesized with 25 terms of the wavelet series, and the synthesized function and its contour plot are shown in Figs. 5 and 6, respectively. Quantitatively, the removal function has been mapped to within a rms error of 3 nm, which is plotted in Fig. 7.
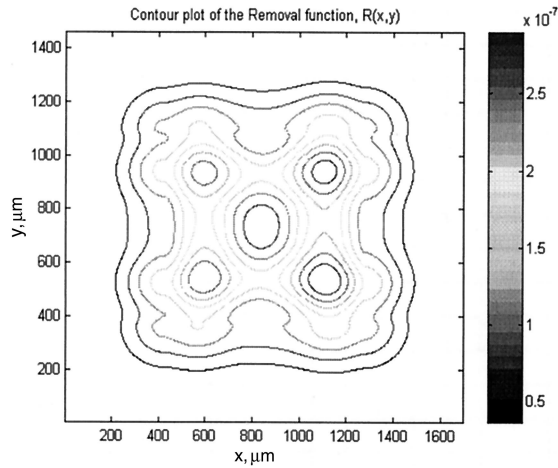
Fig. 6. Contour plot of the removal function $R(x, y)$.

2. Synthesizing the Beam Function $B(x, y)$

The beam function is Gaussianlike, which is circularly symmetric along the X and Y axes. The beam, as shown in Fig. 8, is 120 μm (FWHM) wide along the X and Y axes and has a peak removal rate of 100 nm/min. This function is defined over the same domain as the removal function.

The beam function is synthesized with 25 terms of the wavelet expansion. Since the basis functions of the wavelet expansion are Gaussians and their derivatives, the expansion fits the wavelet expansion accurately to within a few percent with just the first expansion term. The additional terms have been used to satisfy the requirements of the deconvolution algebra, i.e., that both functions (removal and beam) be synthesized with the same number of expansion terms.

3. Deconvolution and the Synthesis of the Dwell Function $D(x, y)$

The dwell function $D(x, y)$ is computed with the wavelet deconvolution algebra described in Subsection 2.D. Note that the computed dwell function, shown in Fig.
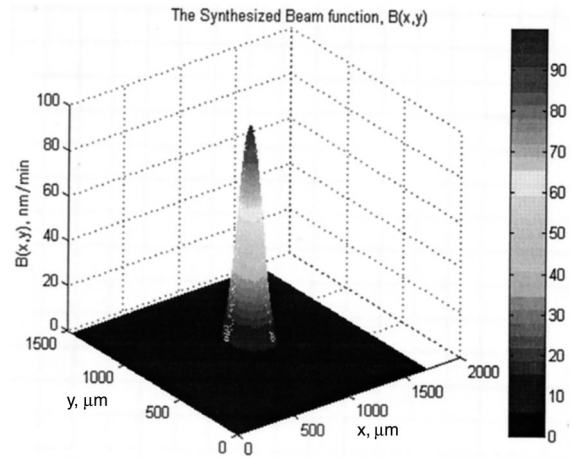

Fig. 8. Synthesized beam function $B(x, y)$.

9, does not resemble the removal contour (Fig. 5) in any way. The contour plot of the dwell function is shown in Fig. 10. The reason for this nonintuitive dwell function is that the 120-μm (FWHM) beam used to figure the removal surface is comparable with the 250-μm dominant spatial period observed in the removal function.

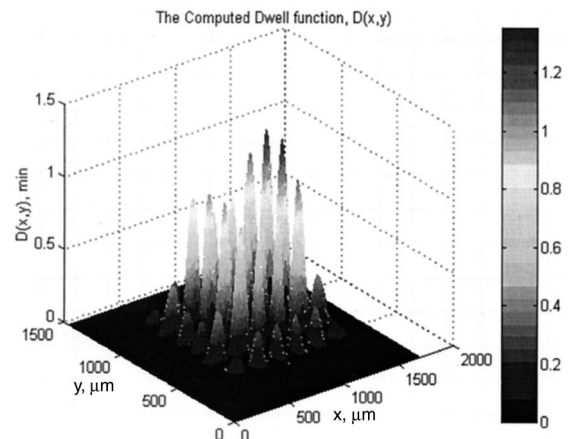Fig. 9. Calculated dwell time $D(x, y)$.

Fig. 7. Variation of the rms error of the synthesized removal function $R(x, y)$.

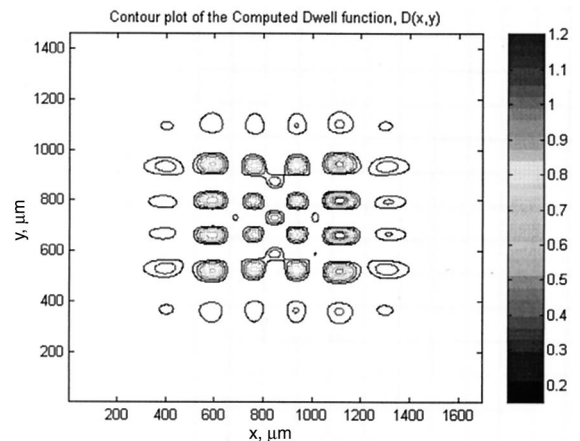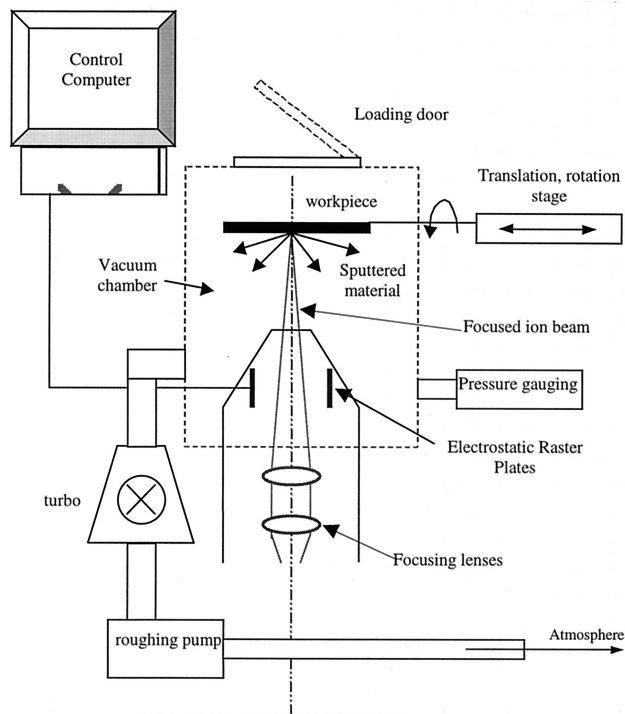Fig. 10. Contour plot of dwell time $D(x, y)$.

Fig. 11.   Schematic of the ion-figuring system.

This simulation clearly indicates the ability of the wavelet algorithm to compute dwell functions for imparting finely detailed removal contours even with relatively wide beams.

4. Ion-Figuring Test Station

A schematic of the ion-figuring system is shown in Fig. 11.   The test station consists of a chamber that houses the duo-plasmatron source, and other peripherals are attached to it, such as pressure gauges and a translation–rotation stage.   Figuring is performed at an operating pressure of approximately 1.3×10^{-5} Torr.   This pressure is achieved and maintained with the standard two-step pumping scheme by roughing and vacuum pumps.   The roughing pump is a dual-seal Welch vacuum pump that roughs the chamber to a pressure of 1×10^{-3} Torr and also provides the same back pressure to a Varian turbomolecular (turbo) vacuum pump.   The turbopump takes over from the roughing pump and pumps down the chamber to a desired operating pressure of 1.3×10^{-5} Torr.   The vacuum inside the chamber and the two pumping lines is monitored with thermocouples and ion gauges.

The duo-plasmatron ion source is attached to the bottom face of the vacuum chamber and is driven by a power supply and controller.   Oryx Instruments built a computer-controlled interface in LabView to monitor and control the ion source remotely.   The beam current of the ion source is collected by a Faraday cup inside the chamber and subsequently measured by a Keithley Instruments electrometer.   The entire system is enclosed within a specially designed box frame assembled from extruded aluminum I-sections.

The chamber is a six-way cast steel cross with the ion source (gun) attached to its bottom face and pointing up.   The low vacuum ($\sim 10^{-3}$ Torr) inside the chamber is monitored with a thermocouple, and a Varian Bayard–Alpert ion gauge is used for a moderate vacuum ($\sim 1\text{-}2 \times 10^{-6}$ Torr).   The vacuum gauges are mounted on the left face of the 6-way cross (viewed from the front).   The front face has a glass blank that serves as a viewport, and the turbopump is mounted to the back face of the chamber.   The sample is loaded inside the chamber from the top through a vacuum-compatible hinged door.

To figure micro-optical components in multiple machining cycles, we need to design a referencing system that locates the beam with respect to the workpiece. One possible design would be to use triangulation: measure the current through three holes (accurately etched outside the useful area of the optic during fabrication).   Once the beam location is determined with respect to these holes, it can be rastered accurately to any position on the substrate.   For initial proof-of-concept machining, the sample was placed on a custom-designed mount.   The mount was fixed to a translation–rotation vacuum-compatible stage, which provided linear motion with a precision of 1 mil and a rotary motion of 360 deg with a precision of 1 deg.

5. Stability of the Duo-Plasmatron Ion Source

The source ideally should produce a beam that remains stable over the entire machining period, which can extend over a period of 10–12 h.   Beam stability can be characterized both by the beam current and by the spatial distribution of the beam.   Both have to remain constant over the entire period to ensure beam stability.

A series of tests were carried out to locate the most stable operating range of the ion source.   For a particular source gas there are numerous parameters, such as source, arc and lens voltages, base and operating pressures, and a voltage drop across the resistor connected to the intermediate electrode (which controls generation of plasma in the high-density region and also the arc current), that govern the stable operation of the gun.   In addition to getting a stable beam, it is also necessary to have sufficient beam current to produce a satisfactory etch rate. (A beam current of $\sim 0.25\text{–}0.5$ μA generates etch rates of approximately 100–200 nm/min.)   A series of parametric tests were conducted in which the above-mentioned parameters were stepped in predetermined increments, and their dependence on the beam current and its stability was monitored over 30-min intervals.

Carefully conducted experiments showed that the beam stability was greatest at low operating pressures of $\sim 1.3 \times 10^{-5}$ Torr, with a base pressure of $\sim 2 \times 10^{-6}$ Torr, and the following voltage settings that are specific to this source:

(1) Source, 3000 V;   (3) lens 1, 2250 V;
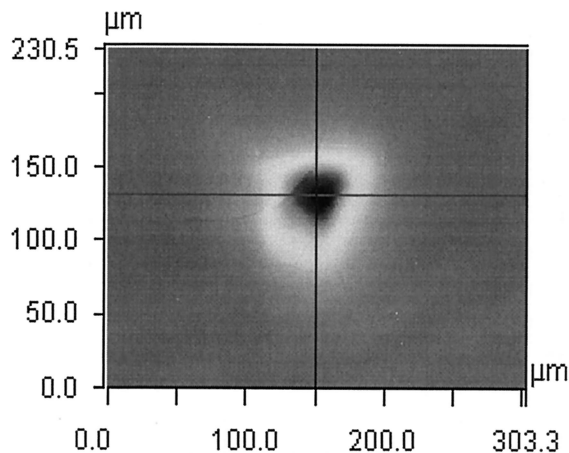(2) arc, 300 V;   (4) lens 2, 1550 V.

Fig. 12.   Contour plot of a typical hole (beam profile) machined in a prepolished silicon substrate.

Fig. 14.   Depth variation along the Y axis (taken at the center) of the hole.

These voltage and pressure settings produced a stable symmetric beam with a beamwidth of ~100-μm FWHM, a beam current of ~0.3 μA, and an etch rate of ~150 nm/min.

The optimum lens voltages (namely, 2250V/1550V) indicate that the beam is focused in the crossover mode. As mentioned above, this mode allows for cleaning the beam spatially by putting in an aperture in the Fourier plane (the focal plane of lens 1).

6.   Figuring Results

Numerous figuring experiments were conducted on initially flat silicon substrates during various stages of development of the ion-figuring system. The two most significant ones are mentioned in Subsection 6.A.

A.   Uniform Depth Profile (Trough)

In this experiment a 1-D uniform depth profile, i.e., a trough, was machined in a 15 mm × 15 mm flat silicon substrate. The profile was machined with a relatively broad beam, shown in Figs. 12–14, namely, 200 μm wide (FWHM) and a peak removal rate of 13

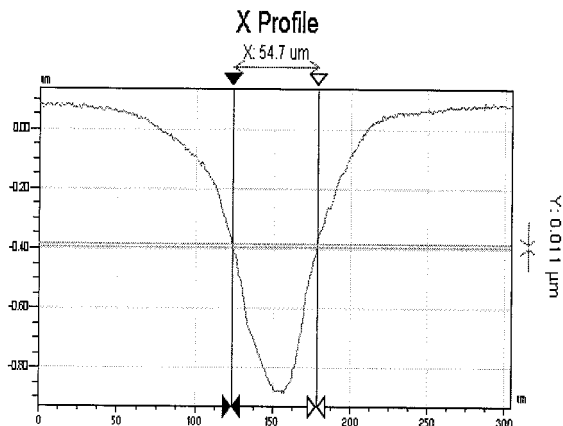nm/min. Figure 15 shows the contour plot of the 1.7-mm-long trough, and the depth profile of the trough is shown in Fig. 16.

The trough was machined by discretizing the work space into 85 segments spaced 20 μm apart and dwelling the beam at the center of each segment for 30 s. The average depth of the trough is 70 nm, and the overall depth error is within ±5% of the maximum height. The actual machining time for this experiment was ~35 min. The rms surface roughness of the silicon substrate before machining was 3 nm, and the postmachining roughness was also 3 nm, which shows that the surface roughness of the substrate is not affected by ion figuring.

B.   Sinusoidal Depth Profile

This experiment was conducted to test implementation of the wavelet algorithm by machining a sinusoidal depth profile in a flat silicon substrate. The depth profile was machined with the dwell map computed by the wavelet algorithm. Since this experiment was also conducted in close succession to the previous one, the same beam parameters (i.e.,
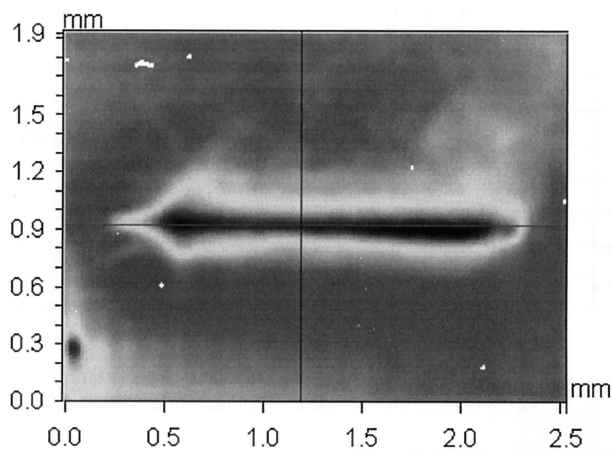

Fig. 13.   Depth variation along the X axis (taken at the center) of the hole.
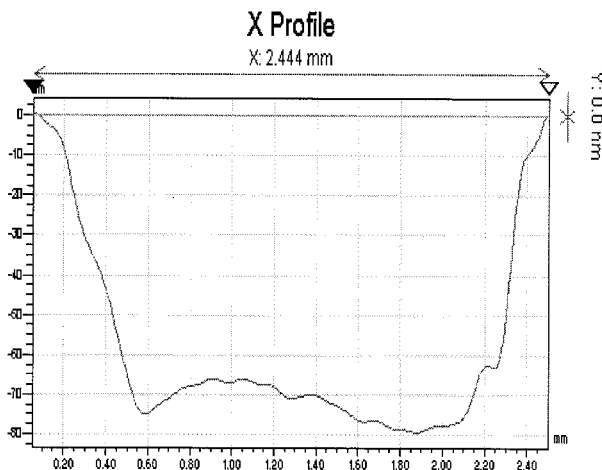

Fig. 15.   Contour plot of the uniform depth profile.

Fig. 16. Depth profile of the trough along its center.

Fig. 19. Desired removal function $R(x)$.

200-μm FWHM and a peak removal rate of 13 nm/min) were used.

The removal function, $R(x)$ as shown in Fig. 15, is a 2-bump sinusoid with an offset of 250 nm and an amplitude of 50 nm. The bumps are periodically spaced 750 μm apart, and the end points of the function are tapered down with a 200-μm (FWHM)

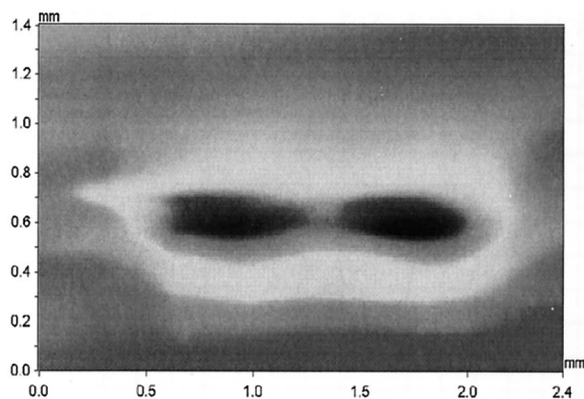Gaussian taper. The actual sinusoid spans a length of 1.5 mm, but with the taper this length extends to 2.4 mm. The deconvolution was performed by discretizing the entire substrate into 281 segments spaced 8.54 μm apart. The dwell function $D(x)$ was obtained by deconvolving the removal function $R(x)$ from the beam function $B(x)$ by wavelet deconvolution techniques. The calculated dwell map was used to control the raster of the beam over the substrate and to generate the desired depth profile.

Figure 17 shows the contour plot of the sinusoidal profile that was machined in ~4 h in the silicon substrate. The depth profile along the center cross section is shown in Fig. 18. A close correlation can be observed between Fig. 18 and the theoretical profile shown in Fig. 19. Quantitatively the profile was figured to within a rms error of 25 nm, which is ~8% of the maximum depth of the sample. The pre and post rms surface roughness was measured to be 3 nm. Also, the figuring rate was observed to be independent of crystal orientation. This experiment demonstrated successful implementation of the wavelet algorithm.

Fig. 17. Contour plot of the figured profile.

7. Summary and Conclusions

An ion-beam-figuring system has been developed for contouring millimeter scale optics. Measured ion-beam functions and desired removal functions were used in a wavelet-based deconvolution algorithm to generate an appropriate dwell function for ion-beam rastering.

Numerous test models were developed to test the stability of the wavelet algorithm. We designed both 1-D and 2-D models for the purpose of understanding the critical parameters of the figuring process and figuring out their interdependence. All 1-D models had a dominant periodicity characterized by λ_{func}. The following trends were observed:

$$\lambda_{taper} \approx 0.75\lambda_{func} \text{ provides a least-fitting error,}$$

$$\lambda_{expn} \approx \lambda_{func} \text{ provides an optimal synthesis.}$$

More terms are necessary to synthesize a function with higher-frequency contour components.

Fig. 18. Experimental removal function $R(x)$.

The actual surface of a 9-element continuous deformable MEMS mirror was used as a test model for 2-D simulations. The mirror surface spanned over an area of 850 μm $\times$ 750 μm and had a maximum height error of 325 nm. This surface, which was synthesized with fundamental widths $\lambda_x = 225$ μm and $\lambda_y = 195$ μm and 25 wavelet terms, was fit to within a rms error of 3 nm. We deconvolved a circularly symmetric 120-μm-wide Gaussian beam function from this removal function to compute the dwell function. The calculated dwell function was nonintuitive and did not resemble the removal function. The beamwidth used in this simulation was comparable with the size of the features on the removal function, which resulted in the nonintuitive dwell function.

As proof of concept, the system was used to contour 15 mm $\times$ 15 mm prepolished silicon substrates. A 1.7-mm uniform depth profile was figured with a 200-μm FWHM beam with a peak removal rate of 13 nm/min. This profile was figured by discretizing the work space into 85 steps of 20 μm each, and the beam was dwelled at the center of each step for 30 s. The maximum depth of the trough was 70 nm, and the depth variation was within $\pm 5\%$ of this maximum depth. A 2-bump sinusoidal depth profile with a maximum depth of 300 nm and a length of 2.4 mm was machined in the silicon substrate. The work space was discretized into 281 segments of 8.04 μm. The dwell function used to figure this profile was computed by the 1-D implementation of the wavelet algorithm. The profile was figured to the desired profile to within a rms error of 25 nm in one iteration. The main source of this error was likely to be changes in the beam function during the course of the machining process. Such changes in beam function were observed in experiments conducted previously on this machine, and the magnitude and time constants associated with this drift were consistent with the figuring error obtained. The figuring rate was observed to be independent of the crystal orientation. Roughness measurements of the premachined and postmachined substrates indicated that ion figuring does not affect surface roughness.

References

1. S. R. Wilson and J. R. McNeil, "Neutral ion beam figuring of large optical surfaces," in *Current Developments in Optical Engineering II*, R. E. Fischer and W. J. Smith, eds., Proc. SPIE **818,** 320–324 (1987).
2. S. R. Wilson, D. W. Reicher, and J. R. McNeil, "Surface figuring using neutral ion beams," in *Advances in Fabrication and Metrology for Optics and Large Optics*, J. B. Arnold and R. E. Parko, eds., Proc. SPIE **966,** 74–81 (1988).
3. L. N. Allen and R. E. Keim, "An ion figuring system for large optic fabrication," in *Current Developments in Optical Engineering and Commercial Optics*, R. E. Fischer, H. M. Pallicove, and W. J. Smith, eds., Proc. SPIE **1168,** 33–50 (1989).
4. L. N. Allen and H. W. Romig, "Demonstration of an ion figuring process," in *Advanced Optical Manufacturing and Testing*, L. R. Baker, P. B. Reid, and G. M. Sanger, eds., Proc. SPIE **1333,** 22–33 (1990).
5. L. N. Allen, J. J. Hannon, and R. W. Wambach, "Final surface error correction of an off-axis aspheric petal by ion figuring," in *Active and Adaptive Optical Components*, M. A. Ealey, ed., Proc. SPIE **1543,** 190–200 (1991).
6. L. N. Allen, R. E. Keim, and T. S. Lewis, "Surface error correction of a Keck 10-m telescope primary mirror segment by ion figuring," in *Advanced Optical Manufacturing and Testing II*, V. J. Doherty, ed., Proc. SPIE **1531,** 195–204 (1991).
7. D. Pileri, "Large optics fabrication: technology drivers and new manufacturing techniques," in *Current Developments in Optical Engineering and Commercial Optics*, R. E. Fischer, H. M. Pallicove, and W. J. Smith, eds., Proc. SPIE **1168,** 25–32 (1989).
8. J. Lubliner and J. E. Nelson, "Stressed mirror polishing: a technique for producing nonaxisymmetric mirrors," Appl. Opt. **19,** 2332–2340 (1980).
9. T. W. Drueding, S. C. Fawcett, S. R. Wilson, and T. G. Bifano, "Neutral ion figuring of CVD SiC," Opt. Eng. **33,** 967–974 (1994).
10. T. W. Drueding, S. C. Fawcett, S. R. Wilson, and T. G. Bifano, "Ion beam figuring of small optical components," Opt. Eng. **34,** 3565–3571 (1995).
11. T. W. Drueding, S. C. Fawcett, and T. G. Bifano, "Contouring algorithm for ion figuring," Precis. Eng. **17,** 10–12 (1995).
12. T. W. Drueding, "Precision ion figuring system for optical components," Ph.D. dissertation (Boston University, Boston, 1995).
13. C. L. Carnal, C. M. Egert, and K. Y. Hylton, "Advanced matrix-based algorithm for ion beam milling of optical components," in *Current Developments on Optical Design and Optical Engineering II*, R. E. Fischer and W. J. Smith, eds., Proc. SPIE **1752,** 54–62 (1992).
14. M. Born and E. Wolf, *Principles of Optics: Electromagnetic Theory of Propagation, Interference and Diffraction of Light* (Cambridge U Press, New York, 1998).
15. B. Wolf, *Handbook of Ion Sources* (CRC Press, Boca Raton, Fla., 1995).
16. T. G. Bifano, R. Mali, J. Perreault, K. Dorton, N. Vandelli, M. Hornstein, and D. Castañon, "Continuous membrane surface micromachined silicon deformable mirror," Opt. Eng. **36,** 1354–1360 (1997).